Published in : International Journal of Thermal Sciences (2018), vol. 134, pp. 639–652
DOI: https://doi.org/10.1016/j.ijthermalsci.2018.08.014
Status : Postprint (Author's version)

TWO-WAY COUPLED SIMULATIONS OF STAGNATION-POINT ABLATION WITH TRANSIENT MATERIAL RESPONSE

Pierre Schrooyen[a,c], Alessandro Turchi[b], Koen Hillewaert[a], Philippe Chatelain[c], Thierry E. Magin[b]

[a] *Cenaero, Rue des Frères Wright, 29, 6041, Gosselies, Belgium*
[b] *von Karman Institute for Fluid Dynamics, Chaussée de Waterloo 72, 1640, Rhode-St-Genèse, Belgium*
[c] *Université catholique de Louvain, Place du Levant 2, 1348, Louvain-la-Neuve, Belgium*

KEYWORDS

Carbon ablation ; Gas-surface interaction ; Fluid-material coupling ; Plasma wind tunnel testing

ABSTRACT

Ablative materials are extensively used in aerospace applications to protect the integrity of the spacecraft during atmospheric entry. Both thermal and mechanical stresses have to be withstood in the severe operating conditions typical of space missions. An accurate modeling of the phenomena taking place when these materials are exposed to such a harsh environment is crucial to ensure the success of future, more demanding, missions. This study aims to couple two tools able to handle two different aspects of the ablative material modeling: a stagnation-line flow solver featuring an integrated ablative boundary condition, and a material response code. The coupling algorithm allows for time accurate solutions of the ablative material thermal response accounting for detailed surface chemistry, in-depth material behavior, and surface recession. Two different coupling strategies have been implemented, based either on a direct or an iterative procedure. The developed tool is used to rebuild plasma wind tunnel experiments performed in the von Karman Institute Plasmatron facility. The outcomes of the two strategies are compared, showing a satisfactory agreement with the experimental data. Among the two analyzed coupling procedures, the direct coupling proved to be computationally less expensive, while conserving the same accuracy of the more complex iterative procedure for the analyzed cases. A sensitivity analysis is also conducted to understand the discrepancy with experimental data and show the effects of four uncertain material parameters: thermal conductivity, density, emissivity, and catalytic efficiency.

Published in : International Journal of Thermal Sciences (2018), vol. 134, pp. 639–652
DOI: https://doi.org/10.1016/j.ijthermalsci.2018.08.014
Status : Postprint (Author's version)

1. Introduction

There are tremendous challenges in the prediction of spacecraft in atmospheric entry to simulate the response of the ablative Thermal Protection System (TPS). This thermal response strongly depends on the interaction between the ablative material of the heat shield and the high-enthalpy flow surrounding the capsule. Requirements concerning mass efficiency for missions with very high entry velocities have led to the development of new classes of light carbon composite ablators. Currently, new physico-chemical models and computational methods are being developed to understand the material response of these new ablators in a hypersonic flow (see for example the review in Refs. [1-3]).

The common approaches for the macroscopic modeling of the TPS material are mainly of three types. The first approach (i) is based on the one- or multi-dimensional transient computation of the in-depth material behavior [4]. The accurate resolution of all processes taking place inside of the material requires complex physical models [5]. However, simplified boundary conditions are usually used for the gas-solid interface in this kind of approach [4]. For instance, inviscid boundary layer edge conditions are taken from separate simplified flowfield simulations, and the surface conditions (i.e., temperature or convective heat flux) are obtained by means of semi-empirical relations. Several material-response codes [6-9] use this approach and Lachaud et al. [2] gives a complete overview of each code capabilities. In the second approach (ii), the surface ablation is treated using a dedicated boundary condition in a Computational Fluid Dynamics (CFD) simulation. This approach has been used extensively in a wide range of applications (i.e., heat shields, solid rocket nozzles, etc.) to study both charring and non-charring materials, using either equilibrium or finite-rate surface chemistry, giving satisfactory results [10-16]. The last, most complex approach, can be described in short as a combination of the previous two. It can be performed either by coupling together two distinct solvers designed to compute the solid side (first approach) and the gas side (second approach) of problem [17,18], or by directly developing a unified numerical tool capable of computing the flow through the material accounting also for in-depth ablation of the material fibers [9,19]. The latter, in particular, is very promising for the study of highly porous materials for which, under certain conditions, the hypothesis of a mere surface ablation is not justifiable [5].

Two separate codes implementing the approach (i) and (ii) to study the ablative material behavior were developed and tested by the authors. First, a numerical tool was developed to solve the steady-state flow along the stagnation-line of pyrolyzing carbon-based materials accounting for the gas-surface interaction (i.e., ablation) and the pyrolysis gas injection [20,21]. In parallel, a material-response code was developed to simulate the complex in-depth thermal response of the same kind of materials [22,23]. The main objective of the present work is to perform and test the implementation of a tool, based on these two codes, capable of performing the third kind of the described approaches (coupled).

The manuscript is organized as follows. In the first part, the capabilities of each code are summarized and the implemented models are reviewed. Then, different coupling strategies are described, tested, and compared using as test cases the experiments performed in the inductively coupled

Published in : International Journal of Thermal Sciences (2018), vol. 134, pp. 639–652
DOI: https://doi.org/10.1016/j.ijthermalsci.2018.08.014
Status : Postprint (Author's version)

Plasmatron facility at the von Karman Institute (VKI). Finally, a sensitivity analysis is performed to put forward the most influencing parameters.

2. Numerical tools

In this section, the two numerical tools (i.e., flow solver and material-response code) used in the analysis are described. The respective models, the boundary conditions, and a verification test case for each code are presented.

2.1. FLOW SOLVER

The surface ablation model used in this study has been implemented in the VKI stagnation-line code [20,21]. The development state of this tool allows CFD steady-state simulations of the flow along the stagnation-line of pyrolyzing carbon-based materials. Only the information relevant for the present gas-surface interaction study are given in the following, interested readers are referred to [20,24] for a more general description of this tool.

2.1.1. MODEL

The stagnation-line governing equations for spherically shaped blunt bodies can be obtained, as described in Ref. [25], by taking the following steps: (i) perform a coordinate transformation to recast the original equations (i.e., cartesian reference frame) in spherical coordinates originating in the body center; (ii) apply a separation $\theta \rightarrow 0$ of variables (i.e., $\hat{\phi}(r,\theta) = \bar{\phi}(\theta)\,\phi(r)$); (iii) take the limit $\theta \rightarrow 0$. In the case of flows in thermal equilibrium and chemical non-equilibrium these equations read

$$\frac{\partial \boldsymbol{U}}{\partial t} + \frac{\partial \boldsymbol{F}}{\partial r} - \frac{\partial \boldsymbol{F^d}}{\partial r} = \tilde{\boldsymbol{S}}, \tag{1}$$

where the vectors of the conservative variables ($\boldsymbol{U}$), the inviscid fluxes ($\boldsymbol{F}$), and the diffusive fluxes ($\boldsymbol{F^d}$) are

$$\boldsymbol{U} = [\rho_i \;\; \rho u \;\; \rho v \;\; \rho E]^T \;\; i = 1, N_S, \tag{2}$$

$$\boldsymbol{F} = [\rho_i u \;\; p + \rho u^2 \;\; \rho uv \;\; \rho uH]^T, \tag{3}$$

$$\boldsymbol{F^d} = \left[-\rho_i u_i^d \;\; \tau_{rr} \;\; \tau_{r\theta} \;\; \tau_{rr} u - Q\right]^T \;\; i = 1, N_S. \tag{4}$$

The vectors in Eqs. (2)-(4) are unaltered with respect to the original system with the following exception: (i) the variables u, v, u_i^d, τ_{rr}, and $\tau_{r\theta}$ only include the part of the original generic variable $\hat{\phi}(r,\theta)$ that depends only on the radial coordinate i.e. $\phi(r)$; (ii) only the radial component of the viscous fluxes is considered because of the flow-field symmetry constraints taken in the ansatz derivation [25]. The source term vector on the right-hand side of Eq. (1) contains, together with the chemical source terms, also the convective and diffusive metric terms arising from the transformation in spherical coordinates.

Published in : International Journal of Thermal Sciences (2018), vol. 134, pp. 639–652
DOI: https://doi.org/10.1016/j.ijthermalsci.2018.08.014
Status : Postprint (Author's version)

The original derivation of the stagnation-line equations given in Ref. [25] assumed the Newtonian theory to express the pressure distribution around the body

$$p - p_\infty = \frac{1}{2} p_\infty u_\infty^2 \cos^2\theta. \tag{5}$$

This assumption provides a good approximation only in the case of hypersonic flows ($Ma \gg 1$). However, the subsonic pressure distribution around a sphere derived from potential flow theory is

$$p - p_\infty = \frac{1}{2} p_\infty u_\infty^2 \left(\cos^2\theta - \frac{5}{4}\sin^2\theta\right), \tag{6}$$

and Eq. (6) reduces to Eq. (5) on the stagnation line ($\theta \rightarrow 0$). Therefore, Eq. (1) still holds in the case of subsonic flows.

The stagnation-line code is coupled with the Mutation^{++} library [26]. The library is used for the computation of the thermodynamic and transport properties, as well as for the evaluation of the gas-phase chemical source terms. Species thermodynamic properties for the present analysis are obtained from the NASA polynomials [27], and relative mixture quantities are derived from pure species quantities through mixing rules. The transport properties are derived from kinetic theory. The chemical production rates for species, based on elementary chemical reactions including third body, are calculated by taking the forward reaction rate coefficients specified by the user in an Arrhenius law form. The backward rate coefficient is determined by satisfying the equilibrium relation.

2.1.2. BOUNDARY CONDITIONS

The boundary condition accounts for the injection of the products of both heterogeneous surface reactions (ablation) and in-depth material decomposition (pyrolysis). The model is based on the following hypotheses: (i) the interaction between the material and the impinging flow takes place only on the surface (no volumetric ablation); (ii) surface mass and energy balances are applied to compute the mass blowing flux and the surface temperature; (iii) the steady-state ablation hypothesis allows to approximate the conductive heat flux through the TPS in order to close the surface energy balance; (iv) the steady-state ablation also permits the evaluation of the pyrolysis mass flow rate as a fixed portion of the mass blowing flux (i.e., at steady state the recession of the surface and that of the char line proceed at the same speed, so the char layer thickness is a constant value); (v) the pyrolysis gas has a prefixed elemental composition and it is injected in thermo-chemical equilibrium at the actual surface conditions (pressure and temperature).

The surface balances over the pyrolyzing ablative material are then given by

$$(\rho_i\, u)_w + \left(\rho_i\, u_i^d\right)_w = \dot{\omega}_{i_w} + \dot{\omega}_{i_g}, \tag{7}$$

$$\underbrace{k_w \left.\frac{\partial T}{\partial r}\right|_w - \sum_i^{N_S} \left(h_i\, \rho_i\, u_i^d\right)_w}_{q_{conv}} + \dot{m}_c (h_c - h_w) + \dot{m}_g \left(h_g - h_w\right) - \sigma\, \varepsilon_w\, T_w^4 = q_{\mathrm{cond,s}}, \tag{8}$$

Published in : International Journal of Thermal Sciences (2018), vol. 134, pp. 639–652
DOI: https://doi.org/10.1016/j.ijthermalsci.2018.08.014
Status : Postprint (Author's version)

where the subscripts g, c, and w indicate the terms that belong to the pyrolysis gas, the charred material, and the gas adjacent to the wall, respectively. Equation (7) is the species surface mass balance ($i = 1, Ns$). In Eq. (7), the species convective flux ($\rho_i\, u$) is triggered by the mass injected into the system. The other terms are, from left to right, the diffusive flux generated by the concentration gradient $\left(\rho_i\, u_i^d\right)$, the source term due to all the surface reactions involving the i^{th} species $\dot{\omega}_{i_w} = \sum_r^{N_r^i} \dot{\omega}_{i\,w}^r$, and the source term due to the pyrolysis gas injection ($\dot{\omega}_{i_g}$). In the surface energy balance, Eq. (8), q_{conv} is the convective heat flux, q_{cond} is the solid heat conduction in the material, h is the enthalpy, and the last term on the left-hand side is the radiative heat flux. Note that the gas radiation is neglected here and the radiative heat flux accounts only for the re-radiation from the hot surface. The term $\dot{m}_c$ is the mass blowing flux due to the surface heterogeneous ablation reactions which consume the material. It corresponds to the sum of all the source terms, $\dot{\omega}_{i_w}$, of those species that participate to the surface reactions. Similarly, $\dot{m}_g$ is the pyrolysis gas mass flux, generated by the in-depth material decomposition and flowing into the boundary layer through the gas-surface interface. In order to close the surface balances, the surface source terms due to the heterogeneous surface reactions have to be computed. Data from Park [28] are used here and the considered reactions are the following: two oxidation reactions ($C_s + O \rightarrow CO$, and $2C_s + O_2 \rightarrow 2CO$), one nitridation reaction ($C_s + N \rightarrow CN$), and one sublimation reaction ($3C_s \rightarrow C_3$).

2.1.3. VERIFICATION

A code-to-code comparison was carried out to verify the ablation model behavior. Reference data were taken from a numerical study on a test conducted in the Interactive Heating Facilities at NASA Ames Research Center [29]. The original graphite body was a 10-deg, one- half-angle sphere cone with a radius of 1.905 cm. Its approximation of a sphere of the same radius to compute the stagnation-point flux through the VKI stagnation-line code was expected not to introduce any significant error. The rebuilt free-stream enthalpy was reported to be approximately 27 MJ/kg, and the measured stagnation-point pressure and cold-wall heat flux were 81 kPa and 21 MW/m^2, respectively. These conditions correspond to the calculated free-stream conditions given in Table 1.

A grid convergence study showed that a mesh composed of 100 cells clustered in the wall region ensures a good resolution of the stagnation point flow. A mixture composed of 11 gas-phase species was considered: C, C_2, C_3, CN, CO, CO_2, N, N_2, NO, O, and O_2. A subset of the gas-phase reactions given in Ref. [30], involving only the selected species, was used to compute the gas-phase chemistry through the Mutation++ library. The obtained results are here compared with those presented in Ref. [29] where the Gauss-Seidel Implicit Aerothermodynamic Navier-Stokes with Thermochemical Surface Boundary conditions (GIANTS) code was used to perform the analysis [31]. Figure 1 shows the mass fraction profiles along the stagnation line obtained from the present simulation, together with the values extracted from Ref. [29]. The two simulations qualitatively agree and the mass fraction profiles show the same behavior despite the pseudo 1D stagnation-line hypothesis, the differences in the diffusion modeling, small discrepancies in the gas-phase chemical reaction rates, and the thermal equilibrium assumption in the present calculation. We note that the species involved in the gas-surface interaction process follow the same behavior giving a qualitative

Published in : International Journal of Thermal Sciences (2018), vol. 134, pp. 639–652
DOI: https://doi.org/10.1016/j.ijthermalsci.2018.08.014
Status : Postprint (Author's version)

evidence of the right implementation of the ablative boundary condition in the VKI stagnation-line code. It is worth noting that the results shown in Ref. [29] were obtained by specifying the experimentally measured surface temperature as opposed to the present calculation, where the surface temperature was directly computed by solving Eq. (8) for a non-pyrolyzing material.

***Table 1**. Freestream conditions for the Arcjet test case from Ref. [29].*

Property	Value
Velocity, m/s	5354
Density, kg/m^3	0.003
Temperature, K	1428
y_{O_2}	0.000
y_{N_2}	0.617
y_{NO}	0.005
y_O	0.121
y_N	0.257

***Figure 1**. Stagnation streamline species mass fraction distribution for the Arcjet test case.*

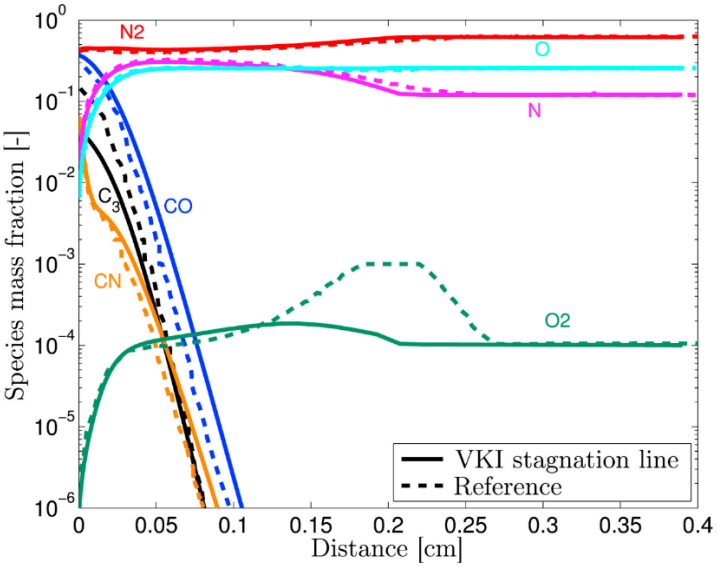

2.2. MATERIAL-RESPONSE CODE

The one-dimensional numerical tool (Echion) uses a Discontinuous Galerkin Method (DGM). This method was introduced back in 1973 by Reed and Hill [32] to solve neutron transport problems. DGM combines the advantages of finite volume and finite element methods. This translates into a high

Published in : International Journal of Thermal Sciences (2018), vol. 134, pp. 639–652
DOI: https://doi.org/10.1016/j.ijthermalsci.2018.08.014
Status : Postprint (Author's version)

accuracy on unstructured meshes, good computational efficiency and scalability due to the locality of data and operations [33]. The use of DGM for an ablative material-response code have already been proposed by Bathia et al. [34-36].

2.2.1. MODEL

According to the categorization of Lachaud [2], the models implemented to treat the complex material thermal response are of type II. For these models, thermal equilibrium between the solid and gaseous phases is assumed, the gas flow inside the porous medium is treated using Darcy's law and only an overall pyrolysis gas mass conservation is solved [7]. The system of equations solved in the ablative material can therefore be written as

$$\frac{\partial \rho_{\mathrm{g}} \epsilon_{\mathrm{g}}}{\partial t} + \frac{\partial (\rho_{\mathrm{g}}\, \epsilon_{\mathrm{g}}\, u_{\mathrm{g}})}{\partial x} = \Pi, \tag{9}$$

$$\frac{\partial \rho_{s_i}}{\partial t} = -A_{s_i} \cdot exp\left(\frac{-E_{a,s_i}}{RT}\right) \rho_0 \left(\frac{\rho_{s_i} - \rho_{r,s_i}}{\rho_{0,s_i}}\right)^{m_{s_i}}, \tag{10}$$

$$u_g = \frac{K}{u_{\mathrm{g}}\, \epsilon_{\mathrm{g}}} \frac{\partial p}{\partial x}, \tag{11}$$

$$\frac{\partial (\rho_{\mathrm{a}} e_{\mathrm{a}})}{\partial t} + \frac{\partial (\epsilon_{\mathrm{g}} u_{\mathrm{g}} \rho_{\mathrm{g}} h_{\mathrm{g}})}{\partial x} = \frac{\partial}{\partial x}\left(k \frac{\partial T}{\partial x}\right), \tag{12}$$

where Eqs. (9) and (10) are the gaseous and solid mass conservation laws, respectively. In Eq. (9), ρ_g stands for the mass density of the gas phase, ϵ_g is the gas volume fraction, and u_g is the interstitial flow velocity within the porous medium. The gas production rate from the decomposition of the solid is Π. This production is computed summing the decomposition of each solid component i (ρ_{s_i} in 7Eq. (10)) given by an Arrhenius law that is usually fitted on thermogravimetry analysis results. In this implementation, the material is supposed to be composed of carbon fibers and a two-component phenolic resin hence the three-component decomposition rate law from Goldstein [37] is used.

The momentum conservation law in the porous medium is restricted to a Darcy's law (see Eq. (11)) where the interstitial velocity is related to the pressure (p) gradient, the viscosity (u_g) and the permeability (κ).

Finally, for the energy conservation law, thermal equilibrium between the fluid and the solid is assumed in the porous medium leading to Eq. (12). The thermal conductivity is noted k and the average specific energy includes the contributions of the solid and gaseous phases

$$\rho_{\mathrm{a}} e_{\mathrm{a}} = \epsilon_{\mathrm{s}} \rho_s e_s + \epsilon_{\mathrm{g}} \rho_g e_g. \tag{13}$$

For pyrolyzing materials, the properties of the solid material such as permeabilities and thermal conductivities are interpolated from the values for pure virgin and charred material,

$$X = \xi_v \cdot X_v + (1 - \xi_v) \cdot X_c, \tag{14}$$

where X stands for a generic properties, the subscripts v and c refer to the virgin and charred material properties, and ξ_v is the fraction of remaining virgin material.

Published in : International Journal of Thermal Sciences (2018), vol. 134, pp. 639–652
DOI: https://doi.org/10.1016/j.ijthermalsci.2018.08.014
Status : Postprint (Author's version)

Several techniques to account for the recession of the computational domain exist. Most material response codes use an *interface tracking* method for which the mesh follows the recession of the material. This category of technique can be subdivided in several types. The first type of method keeps the mesh size constant in the interior domain and modifies it accordingly close to a boundary. Either the position of the first node can be changed [38] or the mesh can be tied to the receding surface and the last node is removed once the recession length exceeds the element size [39]. Removing nodes at the back wall has proved to be more efficient since it removes oscillatory behavior which can occur in this first type of numerical schemes. Within this first category, another method consists in using the Landau coordinate and therefore keeping the number of nodes constant and adjusting the length of the domain.

The present model uses the moving mesh method proposed by Rindall [39] for its ease of implementation. This implies the transformation of the system of equations to a moving coordinate system. For example, the energy equation becomes

$$\frac{\partial(\rho_{\mathrm{a}} e_{\mathrm{a}})}{\partial t} + \frac{\partial(\epsilon_{\mathrm{g}} u_{\mathrm{g}} \rho_{\mathrm{g}} h_{\mathrm{g}})}{\partial x} - \dot{S}\frac{\partial(\rho_{\mathrm{a}} e_{\mathrm{a}})}{\partial x} = \frac{\partial}{\partial x}\left(k\frac{\partial T}{\partial x}\right), \tag{15}$$

where $\dot{S}$ is the recession velocity. During the simulation, once the recession length is larger than an element, the last element (closest to the adiabatic back wall) is removed from the mesh.

In order to solve the problem described by the constitutive laws, the system of equations is decomposed. First the energy and mass density of the solid media are advanced in time with a Super Time Stepping (STS) scheme [40]. Then, the pressure field is found by solving implicitly the gaseous mass conservation where Darcy's law and the perfect gas equation have been used. Finally, the velocity field is updated using the pressure field. At the end of one time step, the mesh is updated to account for the material recession. The different steps and equations solved are summarized in Figure 2 [22].

As shown in Figure 2, the system of equations is split and two time integration schemes are used. The in-depth thermal response is dominated mainly by diffusion terms. The treatment of the diffusion with an explicit scheme entails an unacceptable time step stability constraint. Implicit schemes allow to use a much higher time step at the cost of the solution of a linear system at each time step. An alternative time-integration scheme is the *Super Time Stepping* (STS) scheme that combines a sequence of affordable explicit steps in order to relax the stability constraint [40]. The advantages with respect to implicit schemes are that it is rather easy to implement, and there is no need to derive the jacobian for non-linear cases and to solve the linear system associated with it. Furthermore, Alexiades [40] has shown that the STS can be more advantageous than implicit schemes when one considers the CPU cost-accuracy ratio. These advantages make the method attractive for the first step of our time advancement strategy.

Published in : International Journal of Thermal Sciences (2018), vol. 134, pp. 639–652
DOI: https://doi.org/10.1016/j.ijthermalsci.2018.08.014
Status : Postprint (Author's version)

***Figure 2**. Numerical strategy proposed to solve in-depth thermal response.*

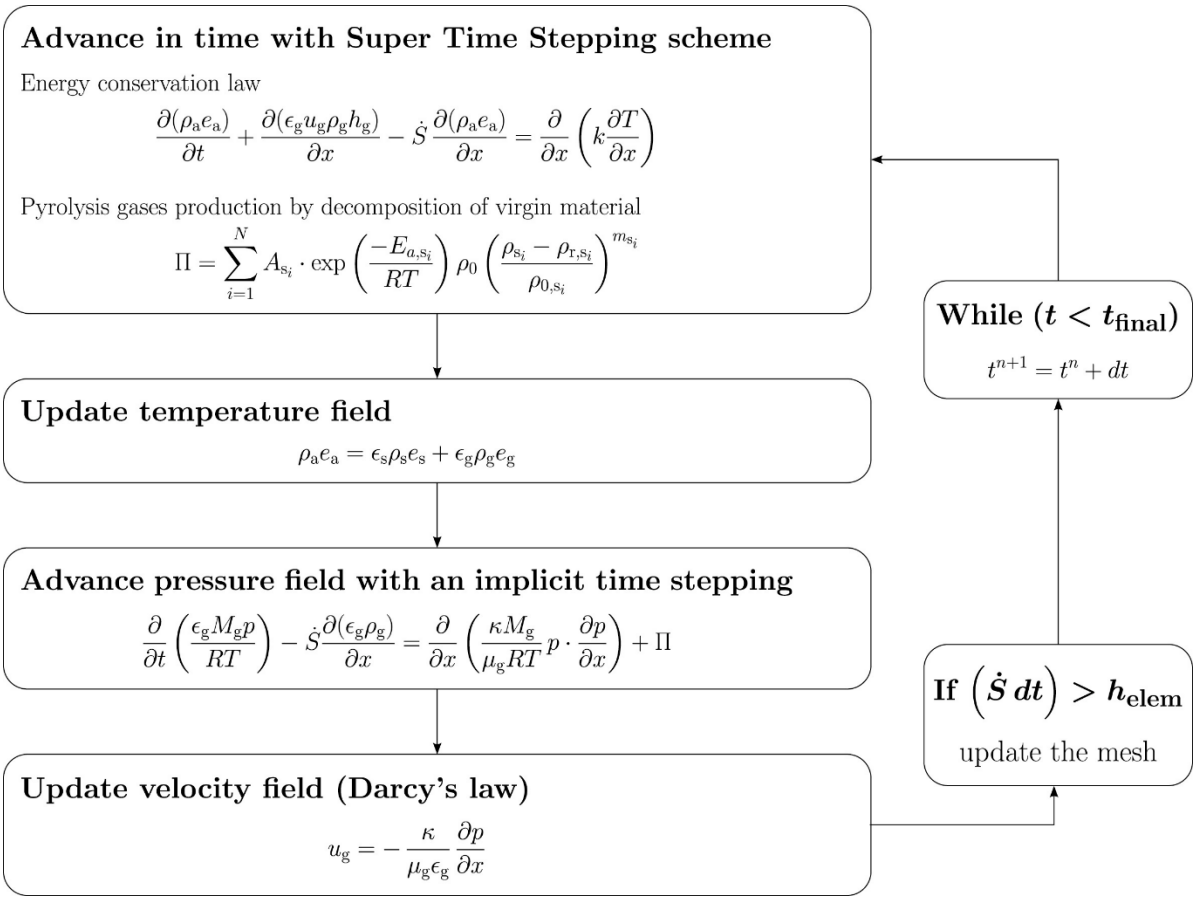

2.2.2. BOUNDARY CONDITIONS

Similarly to the stagnation-line code, Echion can be used as a standalone tool by defining simplified boundary conditions. To account for the chemically reacting boundary layer without solving the flow around the heat shield, it is possible to use mass and energy transfer coefficients at the ablating surface [39]. The energy balance at the wall assuming constant and unitary Lewis and Prandtl number can be written

$$q_{\mathrm{cond,s}} = \rho_e u_e C'_H (h_\mathrm{e} - h_\mathrm{w}) - (\rho u h)_\mathrm{w} + q_{\mathrm{rad_{in}}} - q_{\mathrm{rad_{out}}} + \dot{m}_\mathrm{g} h_\mathrm{g} + \dot{m}_\mathrm{c} h_\mathrm{c}, \tag{16}$$

where C'_H is the Stanton number corrected to account for the blowing at the ablating surface

$$C'_H = C_H \frac{\ln(1+2\lambda B')}{2\lambda B'}, \tag{17}$$

with λ a coefficient depending on the flow regime (0.5 if laminar) and B' a dimensionless mass flow rate.

$$B' = B'_\mathrm{g} + B'_\mathrm{c}, \ with\ B'_\mathrm{g} = \frac{\dot{m}_\mathrm{g}}{\rho_e u_e C_M}\ and\ B'_\mathrm{c} = \frac{\dot{m}_c}{\rho_e u_e C_M}. \tag{18}$$

Published in : International Journal of Thermal Sciences (2018), vol. 134, pp. 639–652
DOI: https://doi.org/10.1016/j.ijthermalsci.2018.08.014
Status : Postprint (Author's version)

2.2.3. VERIFICATION

The code was verified using code-to-code comparisons for test cases with increasing physical complexity, taken from a series proposed by Lachaud et al. [41]. The material used is a Theoretical Ablative Composite for Open Testing (TACOT) with publicly available properties. The code results have been compared for each test case to those obtained with the Pyrolysis and Ablation Toolbox based on OpenFOAM (PATO) [7]. The full verification campaign is presented in Ref. [23]; a representative result is depicted here in Figure 3, where the comparison with PATO for test case 2.3 is shown. For this case, a sample of TACOT is exposed to a given convective heat flux during 60 s and afterwards, re-radiates and ejects gas products. This test case assesses the evolution of the temperature field inside the material, the recession, and the blowing of both the ablated material and pyrolysis gases at the surface. Vertical lines in the temperature field in Figure 3 indicate the successive failures of the virtual thermocouples that occur everytime the recession reaches the thermocouple location. The results for the test case are very close to those obtained with PATO. It should be noted that the mesh has to be sufficiently fine to capture the very stiff gradient at the surface of the material. If the mesh is not sufficiently fine, the high order interpolation may lead to overshoots in the temperature which cause problems in the properties lookup and eventually cause the simulation to stop prematurely.

***Figure 3**. In-depth thermal response of TACOT to a high enthalpy convective boundary condition with recession (Ablation Workshop test case 2.3): comparison of results obtained with Echion compared to those obtained using PATO [42].*

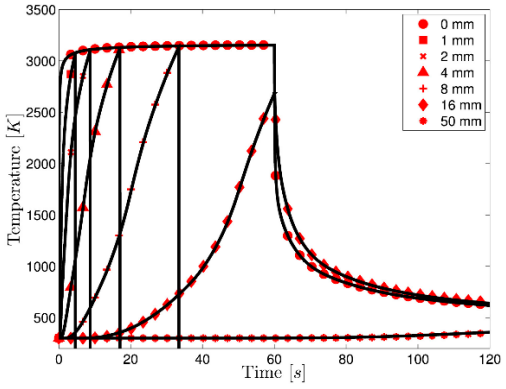

(a) Temperature field for TACOT

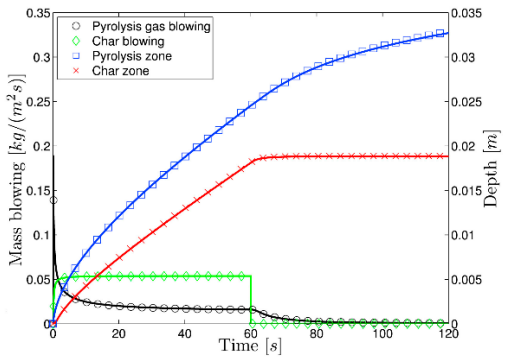

(b) Mass blowing flux and char-virgin zones in the material

Published in : International Journal of Thermal Sciences (2018), vol. 134, pp. 639–652
DOI: https://doi.org/10.1016/j.ijthermalsci.2018.08.014
Status : Postprint (Author's version)

3. Coupled approach

The application of either the flow approach (Section 2.1) or the material one (Section 2.2) provide sufficiently accurate results in numerous cases. However, when the recession rate is high, typically for high velocity atmospheric entry, an accurate analysis of the TPS performances requires a coupled fluid/solid simulation [43]. Indeed, using a decoupled approach, some dynamic interactions cannot be captured accurately. The transfer coefficient approach described in Section 2.2.2 is the most used approach to compute the material transient heating in the absence of more accurate boundary conditions computed by a CFD solver. Similarly, when running the stagnation-line code alone, one has to assume simplifying hypotheses and consider the heat conduction through the material to be steady in order to close the surface energy balance (Eq. (8)). The combination of those tools removes the approximations involved in the two decoupled approaches.

The coupling strategy is a first step to increase the model fidelity of the phenomena at the gas-surface interface. Conti et al. [44] proposed an early attempt to loosely couple Navier-Stokes solutions with material thermal response. The method is based on mass and energy balances at the interface. This kind of coupling strategy allows to use independently two different tools to solve the two sides of the problem and the exchange of the boundary information can be performed only at defined time steps. Throughout the years, several implementation choices have been presented. Differences can be found in the parameters that are exchanged between the codes and in the coupling algorithm definition [17,18,45,46]. Typically, due to the difference in the time scales, pseudo-steady-state CFD computations can combined to transient computations with the material solver to track the evolution of the temperature field inside the solid phase. This strategy is flexible and widely used in the open literature [47,48]; it was considered to be the most suitable method to perform an accurate analysis of the material transient using the present numerical tools. A handler script, responsible for running the two codes and ensuring the data exchange between them, has been conceived and implemented. Details on this coupling algorithm are given in the following.

3.1. EXPLICIT COUPLING

The technique proposed by Chen and Gökçen in Ref. [47] was chosen for its ease of implementation considering the discretization scheme of each code. The total test time is divided in a series of macro time steps ($t_i = t_{i-1} + \Delta t_{\text{macro}}$ for $i = 0, \ldots, n$) and the general logic that applies to each of these steps is as follows: (i) the material-response code solves the transient simulation for a defined macro time step composed by several "internal" time steps for which the STS procedure described in section 2.2 is used; (ii) the temperature of the wall and the total recession are given to the stagnation-line code which updates the CFD domain size and computes the pseudo-steady state solution for these conditions; (iii) the computed convective heat flux and mass blowing flux are exchanged with the material-response code for the next step. When considering pyrolyzing materials, the pyrolysis mass flux provided by the material-response code can be added to the terms exchanged at step (ii). In the present analysis, in which we will rebuild experiments performed on a non-pyrolyzing carbon

Published in : International Journal of Thermal Sciences (2018), vol. 134, pp. 639–652
DOI: https://doi.org/10.1016/j.ijthermalsci.2018.08.014
Status : Postprint (Author's version)

preform, the mass and energy balance (Eqs. (7) and (8)) are modified to omit all the terms that relate to the pyrolysis gas injection. For a non-pyrolyzing material the mass balance, Eq. (7), becomes

$$(\rho_i\, u)_w + \left(\rho_i\, u_i^d\right)_w = \dot{\omega}_{i_w}, \tag{19}$$

where the production rate is depending on the wall temperature given by Echion. The energy balance, Eq. (8), becomes

$$\underbrace{k_w \left.\frac{\partial T}{\partial r}\right|_w - \sum_i^{N_S}\left(h_i\, \rho_i\, u_i^d\right)_w}_{\text{given by CFD solver}_{(\tilde{q}_{\text{conv}})}} - \dot{m}_c h_w + \dot{m}_c h_c - \sigma\, \varepsilon_w\, T_w^4 = q_{\text{cond,s}}, \tag{20}$$

where $\dot{m}_c$ is given by the CFD solver and the term $\dot{m}_c h_w$ is grouped with q_{conv} since it only depends on quantities computed by the fluid solver (this grouped term is named $\tilde{q}_{\text{conv}}$ hereafter). In short, the mass balance, Eq. (19), is solved by the CFD solver while the energy balance, Eq. (20), is solved by the material-response code at every internal time step.

Figure 4 summarizes the different steps. In such a coupling algorithm, each macro time advancement is performed through a full material-code simulation that is run assuming a constant convective heat flux and mass blowing flux. The boundary conditions of the material-response code are therefore assumed piecewise constant over time. The first material-response code simulation is the only exception in this procedure and it is run assuming cold wall conditions and no ablation.

***Figure 4**. Explicit coupling strategy. Each macro time step is composed of one steady-state fluid computation and a time accurate material simulation.*

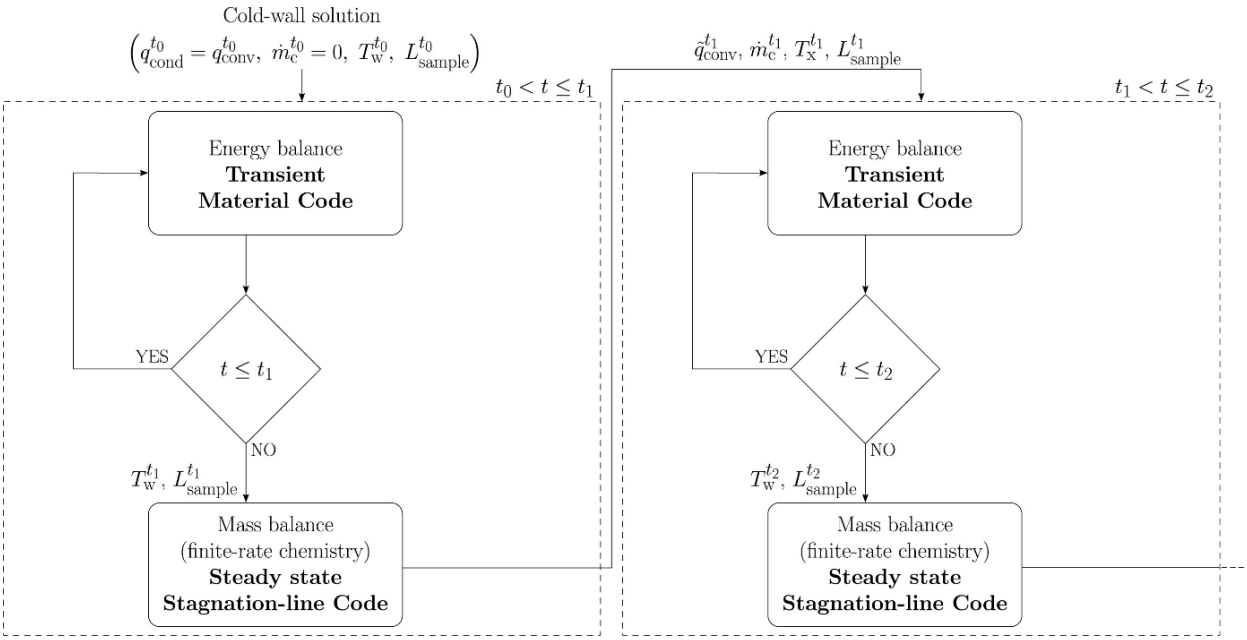

Published in : International Journal of Thermal Sciences (2018), vol. 134, pp. 639–652
DOI: https://doi.org/10.1016/j.ijthermalsci.2018.08.014
Status : Postprint (Author's version)

3.2. IMPLICIT COUPLING

A natural evolution of the previous approach is to upgrade the piecewise constant boundary values exchange between the two codes to a piecewise linear one. This approach follows the idea of Chen and Gökçen [18] to improve the standard explicit coupling. The information-passing sequence and the exchanged parameters are unaltered with respect to the previous algorithm, but a loop is added to account for time varying convective heat flux and mass blowing flux. At each macro time step, the stagnation-line code is run a first time to compute the initial guess of mass blowing flux and convective heat flux (as it is done in the explicit coupling). Then, instead of directly using these values as boundary conditions for the next macro time step, they are linearly interpolated with those computed at the end of the previous macro time step. The time varying boundary condition is assigned to the current material simulation. The new computed wall temperature is then compared with the previous guess and the loop is repeated until convergence is reached. This convergence criterion requires that the temperature difference between two subsequent iterations be less than a predefined value (see Figure 5). This technique should improve the accuracy and the stability of the coupled simulation for a defined set of macro time steps, in particular when dealing with time-varying free- stream conditions (e.g., entry trajectory calculation).

***Figure 5**. Implicit coupling strategy. Several steady state solutions of the flow are used to ensure that the boundary conditions of the material are time accurate.*

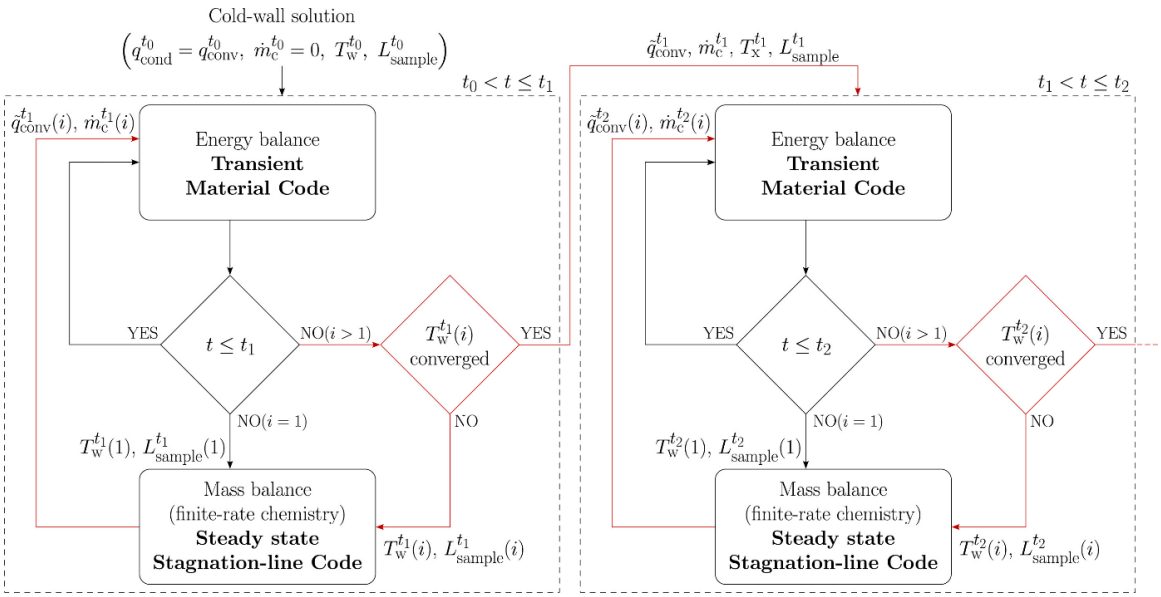

4. Simulation of Plasmatron experiments

The reproduction of the experiments conducted by Helber in the VKI Plasmatron [49] was considered as a suitable test to validate the implemented coupling algorithms. The Plasmatron facility creates a high- enthalpy, highly dissociated subsonic gas flow which can be used to reproduce the

Published in : International Journal of Thermal Sciences (2018), vol. 134, pp. 639–652
DOI: https://doi.org/10.1016/j.ijthermalsci.2018.08.014
Status : Postprint (Author's version)

aerothermodynamic environment of a planetary entry [50]. During Plasmatron TPS experiments, data on surface quantities are provided by a two-color pyrometer (surface temperature) and a high-speed camera (stagnation-point recession). Interested readers are referred to [51,52] for a more thorough explanation of the experimental procedure.

The test conditions from Helber [49] are summarized in Table 2. In the considered experimental tests, the hemispherical sample of 2.5 cm radius was made of Calcarb, a short-fiber carbon preform [53] with a nominal density of 180 kg/m^3. The VKI Rebuilding code [54], which makes use of the experimental measurements, was used to rebuild the boundary-layer edge conditions through the standard procedure used at VKI. These conditions, also shown in Table 2, were used as inlet conditions for the stagnation-line flow computation in which a mixture of 15 species (C, C_2, C_3, CN, CO, CO_2, N, N_2, NO, O, O_2, C^+, N^+, O^+, e^-) was considered. Thermo-chemical equilibrium of this mixture was assumed at the boundary-layer edge, and thermal equilibrium was considered along the stagnation line. For the gas-phase reactions, a subset of the data from Ref. [30] was used in the Mutation^{++} library.

To determine the validity of the assumed hypothesis that the volumetric ablation is negligible and the material removal is a "pure" surface phenomenon, the Thiele number was computed. This non-dimensional parameter indicates the relationship between diffusion and reaction rate in porous media and is defined as

$$Th = \frac{L}{\sqrt{\frac{D_{\mathrm{eff}}}{S_{\mathrm{f}}\, k_{\mathrm{f}}}}} \approx 1e^3, \tag{21}$$

where L is the characteristic length of the sample, D_{eff} is the effective diffusivity, S_{f} is the specific surface of the fibers and k_{f} is the oxidation speed. This value of the Thiele number corresponds to a diffusion limited regime (i.e., a surface ablation regime).

Test P5 is used as the baseline test case. Figure 6 shows the comparison between the three different methods to rebuild the experiment: using the CFD code only, using the material-response code only, or performing the explicit coupling. The two transient solutions were computed either by using only the material-response code with the transfer-coefficient approach or running a coupled CFD/material simulation. The steady-state solution was obtained by using the sole stagnation-line code with the steady-state ablation approximation. As seen, the surface temperature evolution computed by the material-response code using the transfer coefficient approach agrees well with that obtained using the coupled strategy. In Figure 6(b), the total recession computed by the material-response code alone differs from the other two, which are closer to the experimental data. Also, it is worth noting that, for this particular test case, the stagnation-line code alone gives already satisfactory results. However, the critical drawback of this approach is that the transient and the material in-depth temperature field are not computed (i.e., although providing a more accurate description of the gas-surface interaction, the CFD solver alone cannot be used to size the thickness of the heat shield).

Published in : International Journal of Thermal Sciences (2018), vol. 134, pp. 639–652
DOI: https://doi.org/10.1016/j.ijthermalsci.2018.08.014
Status : Postprint (Author's version)

***Table 2**. Nominal Plasmatron test conditions [49] and rebuilt boundary-layer edge conditions.*

	Test ID	P1	P5
Nominal test conditions	Working gas	air	air
	Static pressure, Pa	1500	1500
	Cold-wall heat flux, MW/m^2	1	3
Rebuilt edge conditions	Velocity, m/s	759	1887
	Temperature, K	6228	10587
	Pressure, Pa	1500	1500

***Figure 6**. Comparison between experimental data, material-response code only solution, CFD only solution, and explicit coupling. The experimental curves are the outcomes of optical measurements (i.e., two-color pyrometer and highspeed camera for the surface temperature and the recession, respectively) [52]. The stepwise-constant profile of the recession measurements is due to the high-speed camera resolution. (For interpretation of the references to color in this figure legend, the reader is referred to the Web version of this article.)*

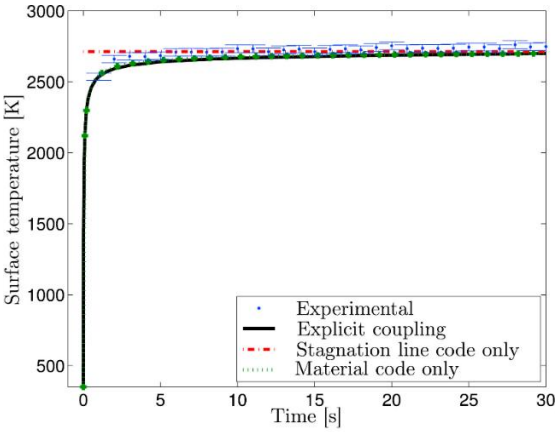

(a) Surface temperature

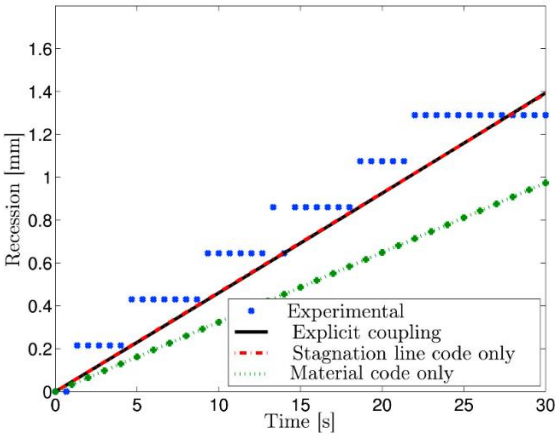

(b) Total recession

Published in : International Journal of Thermal Sciences (2018), vol. 134, pp. 639–652
DOI: https://doi.org/10.1016/j.ijthermalsci.2018.08.014
Status : Postprint (Author's version)

4.1. COMPARISON BETWEEN EXPLICIT AND IMPLICIT COUPLING

The test case presented in Section 4 is used to compare the behavior of the explicit scheme and implicit scheme. Figure 7 shows the difference between the two schemes in terms of wall temperature and temperature field inside the material. The advantages of the implicit scheme in terms of accuracy are negligible in this case. The two simulations show a difference of 4 K on the wall temperature at the end of the transient. As a matter of fact, the piece-wise linear boundary condition assigned to the material-response code did not improve the solution obtained with the computationally cheaper explicit approach. However, it is worth noting that the free-stream conditions of the Plasmatron test are constant over the test duration. We believe that the perfect agreement between the two coupling strategies is a direct consequence of these time-constant test conditions. Indeed, when applying the implicit coupling algorithm, two steady-state CFD simulations were always sufficient to satisfy the chosen convergence criteria of 5 K difference between the computed surface temperatures of two subsequent iterations. In addition, the set of macro-time steps has been chosen in order to capture the transient hence the advantage of increasing the macro-time step using an implicit procedure could not be assessed replicating these experiments. With this in mind, only the cheaper explicit coupling has been used for the following sensitivity analysis.

***Figure 7**. Comparison between implicit (dashed) and explicit (solid) coupling. The internal temperature is shown for increasing time in second (0.01, 0.05, 0.1, 0.2, 0.3, 0.5, 0.8, 1.0, 1.5, 3.0, 5.0, 8.0, 12.0, 18.0, 25.0, 30.0) corresponding to the exchange time between the two codes.*

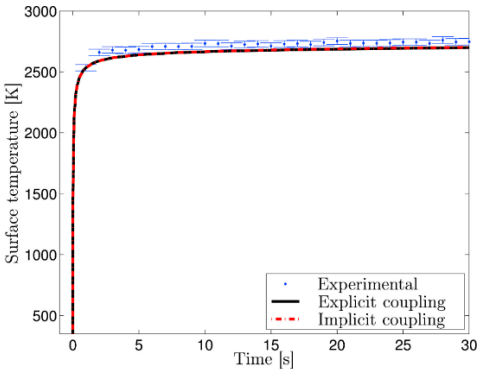

(a) Surface temperature

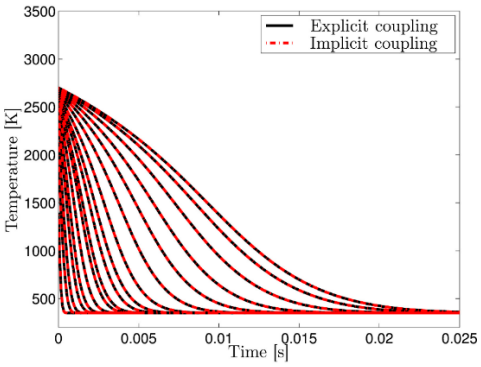

(b) Temperature field for different time

Published in : International Journal of Thermal Sciences (2018), vol. 134, pp. 639–652
DOI: https://doi.org/10.1016/j.ijthermalsci.2018.08.014
Status : Postprint (Author's version)

4.2. SENSITIVITY ANALYSIS

The difference observed in Figure 6 between the numerical results and the experimental data might be explained by the uncertainty on several important parameters. Within this section, the effect of four different material properties are investigated. The first two are in-depth properties: thermal conductivity and density. The last two influence mostly the surface energy and mass balance: emissivity and catalytic efficiency. Their influence on the wall temperature, total recession, and temperature field within the material is studied.

4.2.1. THERMAL CONDUCTIVITY

Thermal conductivity has a strong impact on the heat transfer through the solid material in the transient phase. This, together with its objectively difficult characterization because of the complex porous structure of light ablators, make this property a prime candidate for the sensitivity analysis. The thermal conductivity provided by the manufacturer of Calcarb [53] varies by a factor of two, depending on the type of measurements (laser diffusivity measurement or hot plate technique). Moreover, the range of temperatures does not cover the experimental temperature range for the Plasmatron experiment and necessitated an extrapolation of the data in the baseline analysis (Section 4). A simulation using TACOT conductivity has been run to investigate the effect of this parameter on the final results. The evolution of the different thermal conductivities with respect to the temperature is shown in Figure 8.

The influence on wall temperature, recession and in-depth thermal response are shown in Figures 9 and 10. As expected, the conductivity influences mainly the temperature field inside the material without really impacting the surface quantities. We recall that, theoretically, the thermal conductivity value can have an impact on the surface values during the transient, however the strong heating rate of the present test case seems to nullify this effect. In the future, it would be interesting to have thermocouple data inside the material to compare with the computed temperature field, as well as analyzing test cases with less steep heating rates.

***Figure 8**. Thermal conductivity with respect to temperature. Measured data [53] (two different measurement techniques) and charred TACOT thermal conductivity from Ref. [42] are compared.*

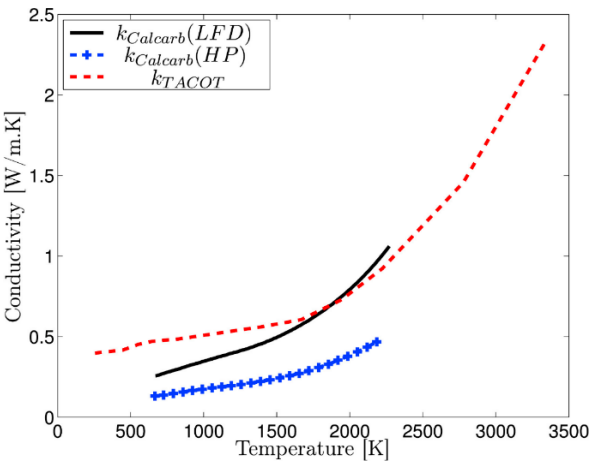

Published in : International Journal of Thermal Sciences (2018), vol. 134, pp. 639–652
DOI: https://doi.org/10.1016/j.ijthermalsci.2018.08.014
Status : Postprint (Author's version)

***Figure 9**. Surface temperature and total recession for different thermal conductivities.*

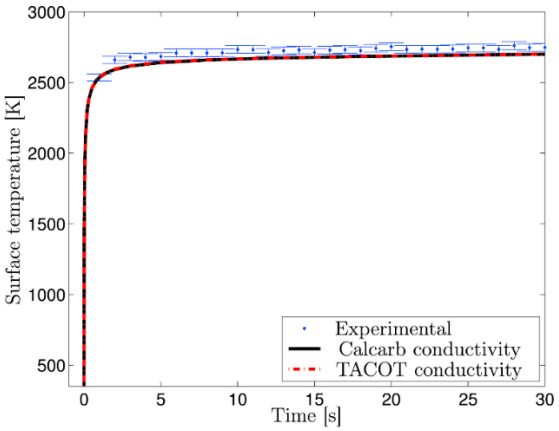

(a) Surface temperature

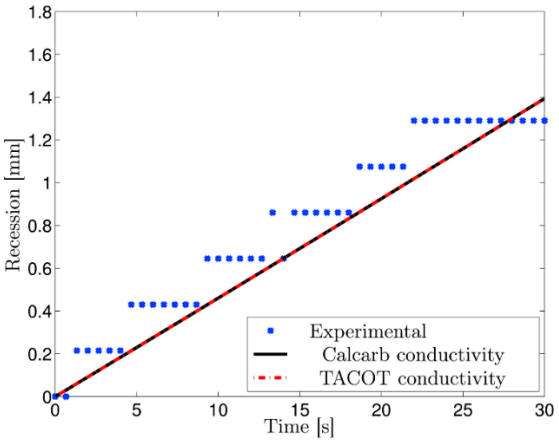

(b) Total recession

***Figure 10**. Temperature field for different time. Solid lines are the reference results, dashed lines are the results with different conductivity.*

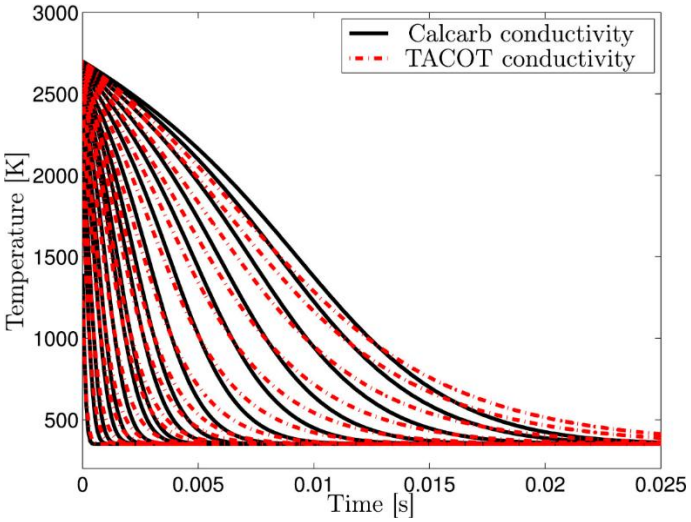

Published in : International Journal of Thermal Sciences (2018), vol. 134, pp. 639–652
DOI: https://doi.org/10.1016/j.ijthermalsci.2018.08.014
Status : Postprint (Author's version)

4.2.2. DENSITY

The nominal density of the material, as reported in the manufacturer brochure [53], is 180 kg/m^3. However, analysis performed at VKI by Helber [49] showed substantial variations of this material characteristic for the analyzed samples. The material density has a strong impact on the quantities of interest of the present analysis mainly for two reasons: (i) the ablative boundary condition of the stagnation-line code returns the value of the mass blowing flux that has to be converted into a surface recession rate by the material-response code through the material density; (ii) the density has a direct impact on the thermal diffusivity of the material, which affects the in-depth temperature field development. From the results by Helber [49,52] a density value of 215 kg/m^3 was chosen as an alternative value for the sensitivity analysis. Figures 11 and 12 show the impact of this property on both the surface quantities and the internal temperature field. As shown, the wall temperature is not dependent on this parameter; however, the recession is directly related to the density for the reasons explained above. The change in the thermal diffusivity affects the temperature field inside the material by delaying its heating. Interestingly, the effect of the density, through the thermal diffusivity, looks qualitatively different than the effect of the thermal conductivity shown in Figure 10. The latter appears as a modification of the conductive heat flux because of the induced slope change of the temperature profile, whereas the former really looks like a delay in the thermal wave evolution represented by a shift in the temperature profiles.

***Figure 11**. Surface temperature and total recession for different material densities.*

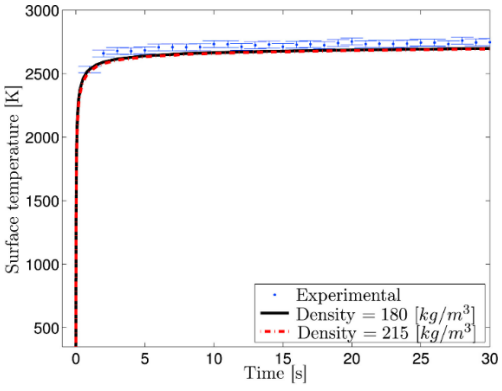

(a) Surface temperature

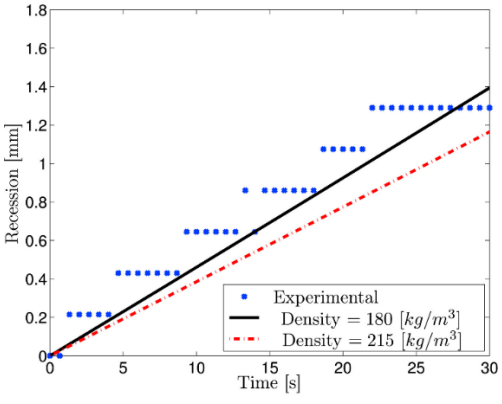

(b) Total recession

Published in : International Journal of Thermal Sciences (2018), vol. 134, pp. 639–652
DOI: https://doi.org/10.1016/j.ijthermalsci.2018.08.014
Status : Postprint (Author's version)

***Figure 12**. Temperature field for different time. Solid lines are the reference results, dashed lines are the results with different density.*

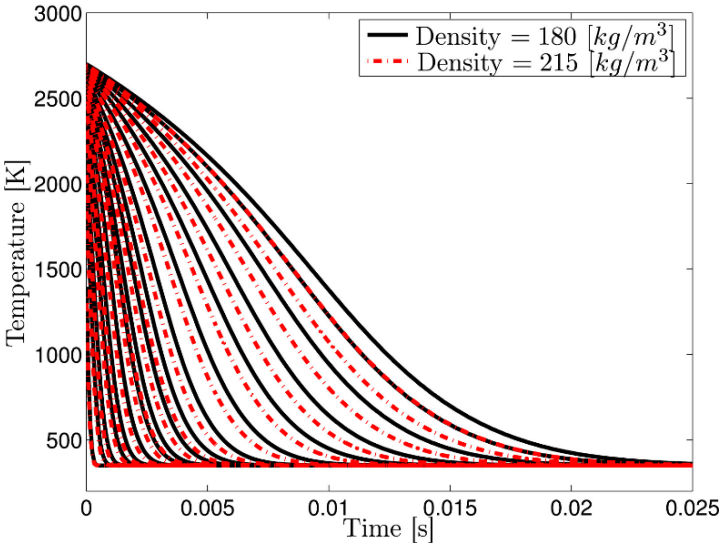

4.2.3. EMISSIVITY

An important parameter in Eq. (8) is the integral emissivity of the surface. This parameter is necessary to compute the heat lost by the surface because of the re-radiation towards the surrounding environment. A single value, independent on the surface temperature, is considered in the model. In the baseline analysis, Section 4, the value of $\epsilon_w = 0.86$ was used. This value, given by Helber [49] for the material under investigation, was obtained by combining the independent emissivity measurement of the surface temperature, made through the two-color pyrometer, with an additional temperature measurement performed using an infrared radiometer. However, in Ref. [49] a non- negligible spread in the computed emissivity values is shown for the material with values down to 0.8. Furthermore, other studies pointed out that the roughness of the surface generated and enhanced by ablation will strongly affect the emissivity measurement [55]. Although very low values were measured in Ref. [55] for surface with different polishing levels, it is believed that for the high surface temperature range of the present test and the rough surface of the test specimen, the measured range 0.80-0.86 can be considered the most probable for the emissivity. Therefore, an additional emissivity of 0.8 was tested. Figures 13 and 14 show the computed surface quantities and the in-depth temperature field, respectively. The effect of the reduced emissivity is evident in the surface quantities. The emissivity value of 0.8 causes a slight increase in the surface temperature giving excellent agreement with the experimental data and a negligible variation in the recession.

Published in : International Journal of Thermal Sciences (2018), vol. 134, pp. 639–652
DOI: https://doi.org/10.1016/j.ijthermalsci.2018.08.014
Status : Postprint (Author's version)

***Figure 13**. Surface temperature and total recession for different emissivities.*

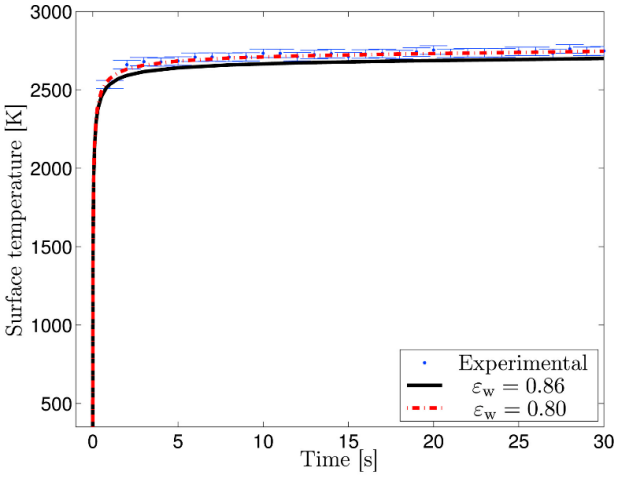

(a) Surface temperature

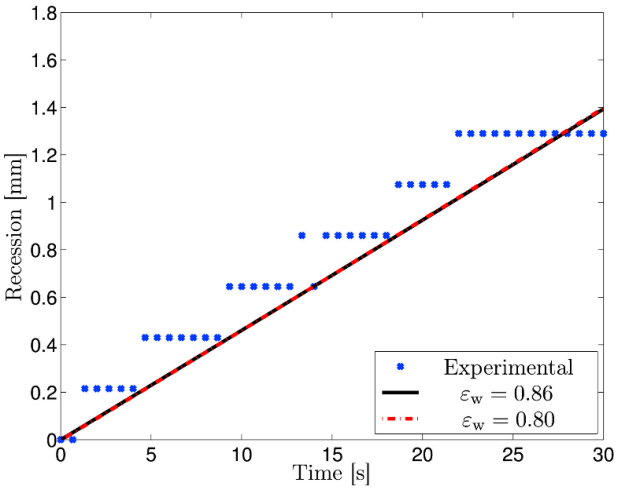

(b) Total recession

***Figure 14**. Temperature field for different time. Solid lines are the reference results, dashed lines are the results with different emissivities.*

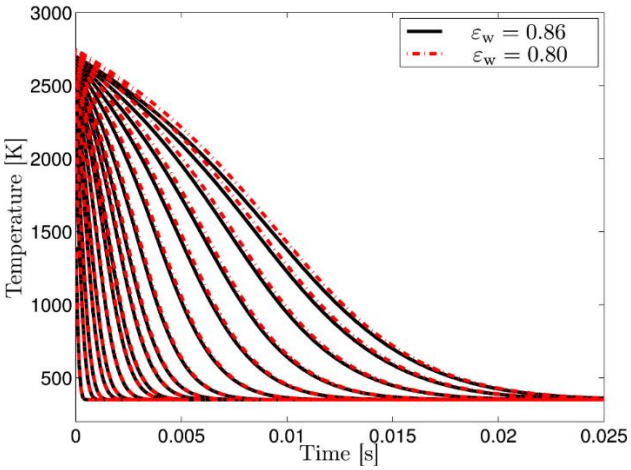

Published in : International Journal of Thermal Sciences (2018), vol. 134, pp. 639–652
DOI: https://doi.org/10.1016/j.ijthermalsci.2018.08.014
Status : Postprint (Author's version)

4.2.4. CATALYTIC REACTIONS AT THE SURFACE

When dealing with ablative materials, the heterogeneous reactions produce the mass loss that has been extensively analyzed throughout the present work. However, when a non-equilibrium mixture impinges on a surface, ablative or not, heterogeneous atomic recombinations can take place because of the catalyzing effect of surface active sites. Although these surface reactions are normally neglected when ablative surface are considered, there is typically little arguments to justify this choice. This is particularly true for nitrogen recombination that is likely to have an impact i) because the nitrogen concentration at the wall is not negligible due to the low reaction efficiency of the other surface reaction. A recent experimental/numerical study [56] tried to characterize the ablative and catalytic behavior of light-weight carbon-based ablators when exposed to nitrogen plasmas finding that catalytic recombination might be significant. On the contrary, the case of oxygen is different as modern molecular beam experiments [57] found no evidence of O atom recombination on an ablating carbon surface. Numerically, there were few attempts to study the influence of catalytic recombination on ablators. Driver et al. [58] tested a range of catalytic recombination efficiencies with values as high as 0.5 to match arc-jet data. consuming the atomic nitrogen in the gas: the nitridation; ii) due to its high exothermicity. Turchi et al. [59,60] showed that a complex interaction exists between the surface nitrogen recombination and the nitridation reaction, which has a non-negligible impact on the outcomes of the present surface ablation model. Moreover, values different than zero for the recombination probability of atomic nitrogen are included in the most up-to-date gas-surface interaction models [18]. For all these reasons, a reaction probability value of 0.05 was selected for the present analysis.

Figure 15 shows the influence of the enabled surface catalytic efficiency on the surface temperature and recession rate. The exothermic process implies a rise of the surface temperature which over predicts the experimental profile. Despite the temperature rise of around 200 K, the surface recession is only slightly increased as a consequence of the diffusion-limited regime of the surface oxidation (main contributor to the mass loss) in the present condition. This small increase in the recession gives a better agreement with the measured one. Figure 16 shows the in-depth temperature field. The higher surface temperature produces a sensible change in the internal temperature profile. However, the differences seem to reduce more in depth where the obtained temperature profiles are still comparable. The large impact of the catalytic efficiency on the wall temperature shows the importance of characterizing this parameter accurately.

Published in : International Journal of Thermal Sciences (2018), vol. 134, pp. 639–652
DOI: https://doi.org/10.1016/j.ijthermalsci.2018.08.014
Status : Postprint (Author's version)

***Figure 15**. Surface temperature and total recession for different catalytic efficiencies.*

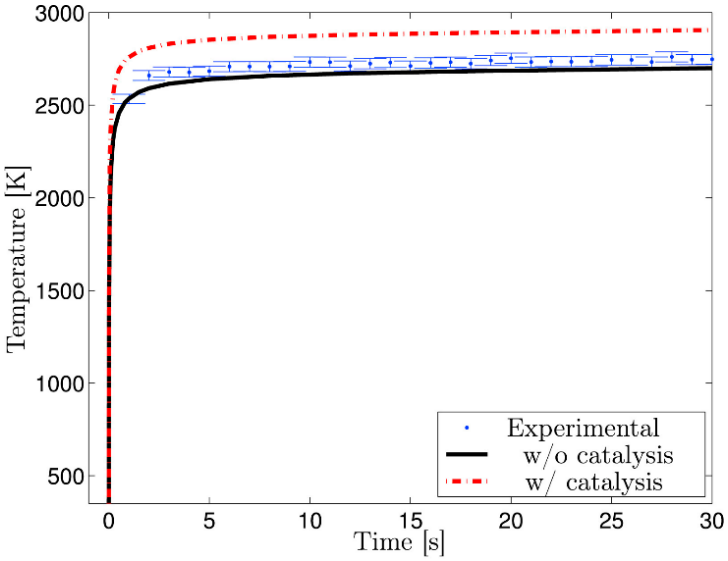

(a) Surface temperature

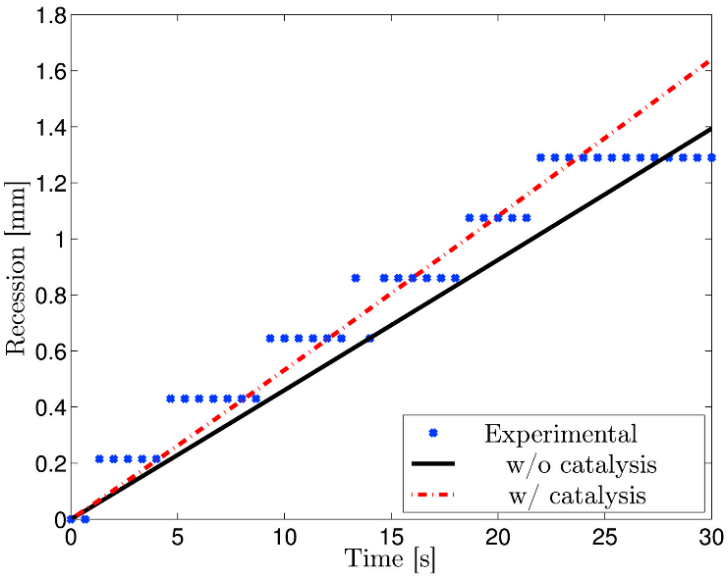

(b) Total recession

Published in : International Journal of Thermal Sciences (2018), vol. 134, pp. 639–652
DOI: https://doi.org/10.1016/j.ijthermalsci.2018.08.014
Status : Postprint (Author's version)

***Figure 16**. Temperature field for different time. Solid lines are the reference results, dashed lines are the results with catalytic efficiency.*

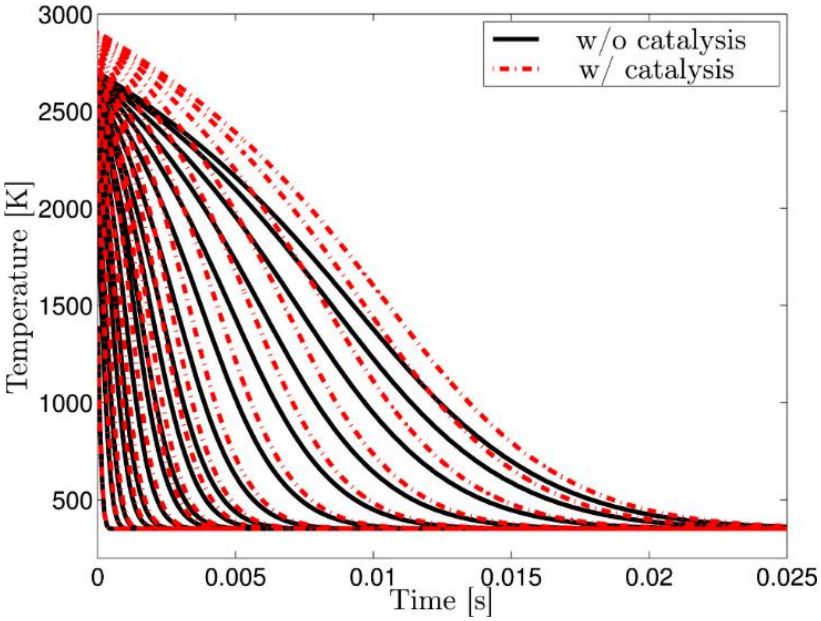

4.3. TEST CASE P1

Test P1 of Table 2 was also analyzed. Nitrogen surface recombination was investigated also in this case, and the same value of reaction probability considered for test P5 (Section 4.2.4) was used. The results in Figure 17 show a similar trend as for P5: the catalycity slightly affects the recession but substantially changes the computed surface temperature.

Analyzing these results, and comparing them to the experimental data, the catalycity seems to be a "free parameter" that would allow to match the outcomes of both tests. However, it is evident that to match these data a non-negligible catalytic efficiency has to be considered only in the low heat-flux condition (test P1). A short literature survey reveals that many models describing the evolution of the recombination efficiency with temperature, consider a strong decrease of this efficiency for temperatures above a particular threshold value (depending on the analyzed material) [61-63]. A similar phenomenon was also observed experimentally in Ref. [64]. A first explanation of this could be found in the possible change of the recombination reaction order, that above a critical value of the temperature can switch from first to second order with a squared dependence on pressure [62]. Alternatively, it can be attributed to a stronger thermal desorption of the absorbed atoms at higher temperature that can deplete significantly the surface coverage [61,63]. In view of the present analysis we suggest that if a similar behavior occurs also in the case of ablative materials, it can significantly affect the material-response analysis.

Published in : International Journal of Thermal Sciences (2018), vol. 134, pp. 639–652
DOI: https://doi.org/10.1016/j.ijthermalsci.2018.08.014
Status : Postprint (Author's version)

***Figure 17**. Surface temperature and total recession for a lower heat flux experiment (test P1 in Table 2).*

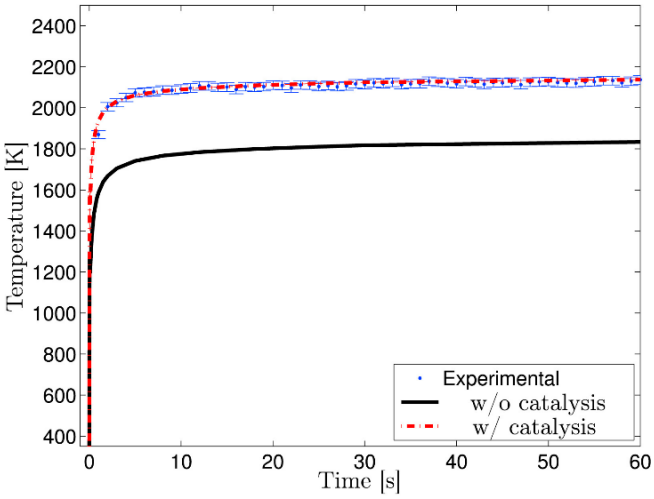

(a) Surface temperature

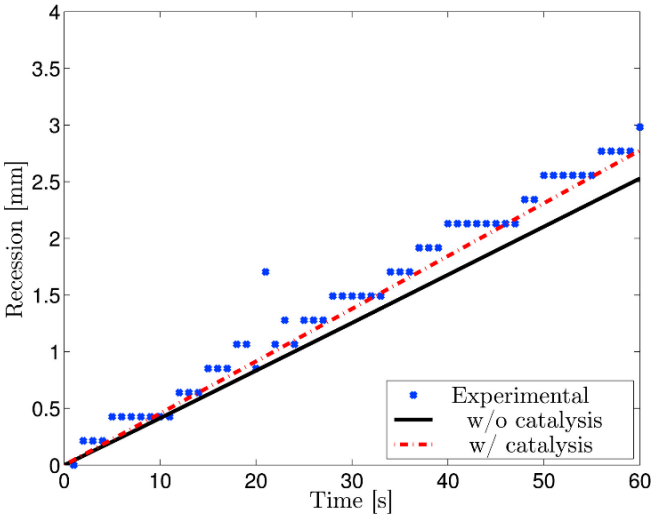

(b) Total recession

5. Conclusions

A study of the transient behavior of ablative thermal protections exposed to reentry-like conditions has been presented. This was performed by coupling, through a boundary-value information passing procedure, two separate tools that solve the flow side and the material side of the problem, respectively. Particular attention was paid to the selection of the best coupling algorithm. Two different procedures were implemented and tested, namely a direct one (explicit) and an iterative one (implicit).

The presented validation test cases aimed at simulating the plasma wind tunnel experiments performed in the von Karman Institute inductively coupled Plasmatron facility. These tests included

Published in : International Journal of Thermal Sciences (2018), vol. 134, pp. 639–652
DOI: https://doi.org/10.1016/j.ijthermalsci.2018.08.014
Status : Postprint (Author's version)

both a high (3 MW/m^2) and a low heat-flux (1 MW/m^2) condition. Our computations showed the advantages of using a coupled approach to reproduce such experiments. Among the two analyzed coupling procedures, the explicit coupling proved to be computationally less expensive, while conserving the same accuracy of the more complex implicit procedure for the analyzed cases.

A sensitivity analysis of the most probably uncertain input parameters for the models was also performed. Both bulk properties (i.e., material density and material thermal conductivity) and surface properties (i.e., integral emissivity and surface catalytic efficiency) were considered in this analysis. We analyzed their effects on three quantities of interest: the wall temperature, the material recession, and the indepth temperature distribution. Our results showed that the material density can affect directly both the computed recession velocity and the in-depth temperature profile. In particular, for the latter, the thermal wave is delayed due to the modified thermal diffusivity. Differently, the considered surface quantities have a strong impact on the surface temperature and, as a consequence, on the in-depth temperature field. As expected, the thermal conductivity affects only the in-depth temperature profile without altering the final (steady-state) value of the surface temperature.

Overall, the coupled procedure showed the ability to compute quite accurately the surface recession, which seems to be quite insensitive to the parametric analysis for both the analyzed test cases. Results obtained with the baseline data are in very good agreement with the experimental surface temperature for the high heat-flux condition. However, for the analyzed low heat-flux condition, the agreement obtained using the baseline input parameters is not as much satisfactory, and the surface catalytic efficiency has been identified as the potentially influential parameter.

Additional experimental data, such as thermocouple measurements, would be useful in the future to identify and quantify the exact role of these parameters. Rebuilding of other plasma wind tunnel tests would help in both rigorously validating the coupled tools and subjecting the coupling schemes to more stressful tests that would differenciate them.

ACKNOWLEDGMENTS

Pierre Schrooyen was supported by a fellowship from the Fund for Research Training in Industry and Agriculture (FRIA). The research of Alessandro Turchi and Thierry E. Magin was supported by the European Research Council Starting Grant #259354. The authors would like to thank N. Mansour for hosting them at the NASA Ames Research Center where this work was performed. Special thanks go to B. Helber for providing us with the experimental data, and J. Lachaud for valuable discussions.

Published in : International Journal of Thermal Sciences (2018), vol. 134, pp. 639–652
DOI: https://doi.org/10.1016/j.ijthermalsci.2018.08.014
Status : Postprint (Author's version)

References

[1] M. Wright, M. Hughes, A. Calomino, M. Barnhardt, An overview of technology investments in the NASA entry systems modeling project, 53rd AIAA Aerospace Sciences Meeting, no. AIAA 2015-1892, 2015 Kissimmee, FL.

[2] J. Lachaud, T. Magin, I. Cozmuta, N. Mansour, A short review of ablative material response models and simulation tools, 7th European Aerothermodynamics Symposium, Brugge, 2011.

[3] G. Duffa, Ablative Thermal Protection Systems Modeling, American Institute of Aeronautics and Astronautics, Inc., Reston,Virginia, 2013.

[4] E.P. Bartlett, R.M. Kendall, C.B. Moyer, R.A. Rindal, An Analysis of the Coupled Chemically Reacting Boundary Layer and Charring Ablator, Part 1 Summary Report, Contractor Report CR-1060, NASA, June 1968.

[5] J. Lachaud, I. Cozmuta, N.N. Mansour, Multiscale approach to ablation modeling of phenolic impregnated carbon ablators, J. Spacecraft Rockets 47 (6) (2010) 910–921, https://doi.org/10.2514/1.42681.

[6] Y.-K. Chen, F. Milos, T. Gökçen, Validation of a three-dimensional ablation and thermal response code, 10th AIAA/ASME Joint Thermophysics and Heat Transfer Conference, 2010 no. AIAA 2010-4645, Chigaco, IL.

[7] J. Lachaud, N. Mansour, Porous-material analysis toolbox based on OpenFoam and applications, J. Thermophys. Heat Tran. 28 (2) (2014) 191–202, https://doi.org/10.2514/1.T4262.

[8] J. Dec, R. Braun, B. Laub, Ablative thermal response analysis using the finite element method, J. Thermophys. Heat Tran. 26 (2) (2012) 201–212, https://doi.org/10.2514/1.T3694.

[9] H. Weng, A. Martin, Multidimensional modeling of pyrolysis gas transport inside charring ablative materials, J. Thermophys. Heat Tran. 28 (4) (2014) 583–597, https://doi.org/10.2514/1.T4434.

[10] F. Milos, D.J. Rasky, Review of numerical procedures for computational surface thermochemistry, J. Thermophys. Heat Tran. 8 (1) (1994) 24–34, https://doi.org/10.2514/3.497.

[11] Y. Chen, F. Milos, Navier-Stokes solutions with finite rate ablation for planetary mission earth reentries, J. Spacecraft Rockets 42 (6) (2005) 961–970, https://doi.org/10.2514/1.12248.

[12] D. Bianchi, F. Nasuti, E. Martelli, Navier-Stokes simulations of hypersonic flows with coupled graphite ablation, J. Spacecraft Rockets 47 (4) (2010) 554–562, https://doi.org/10.2514/1.47995.

[13] D. Bianchi, F. Nasuti, E. Martelli, Thermochemical erosion analysis for graphite/carbon-carbon rocket nozzles, J. Propul. Power 27 (1) (2011) 197–205, https://doi.org/10.2514/1.47754.

[14] P. Thakre, V. Yang, Chemical erosion of carbon-carbon/graphite nozzles in solid-propellant rocket motors, J. Propul. Power 24 (4) (2008) 822–833, https://doi.org/10.2514/1.34946.

[15] A. Turchi, D. Bianchi, F. Nasuti, M. Onofri, A numerical approach for the study of the gas-surface interaction in carbon-phenolic solid rocket nozzles, Aero. Sci. Technol. 27 (2013) 25–31, https://doi.org/10.1016/j.ast.2012.06.003.

[16] D. Bianchi, A. Turchi, M. Nasuti, F, Onofri, Chemical erosion of carbon-phenolic rocket nozzles with finite-rate surface chemistry, J. Propul. Power 29 (5) (2013) 1220–1230, https://doi.org/10.2514/1.B34791.

[17] D. Bianchi, A. Turchi, F. Nasuti, M. Onofri, Coupled CFD analysis of thermochemical erosion and unsteady heat conduction in solid rocket nozzles, 48th AIAA/ASME/SAE/ASEE Joint Propulsion Conference and Exhibit, 2012 no. AIAA 2012–4318, Atlanta, GA.

[18] Y.-K. Chen, T. Gökçen, Implicit coupling approach for simulation of charring carbon ablators, J. Spacecraft Rockets 51 (3) (2014) 779–788, https://doi.org/10.2514/1.A32753.

[19] P. Schrooyen, K. Hillewaert, T. Magin, P. Chatelain, Fully implicit discontinuous Galerkin solver to study surface and volume ablation competition in atmospheric entry flows, Int. J. Heat Mass Tran. 103 (2016) 108–124, https://doi.org/10.1016/j.ijheatmasstransfer.2016.07.022.

Published in : International Journal of Thermal Sciences (2018), vol. 134, pp. 639–652
DOI: https://doi.org/10.1016/j.ijthermalsci.2018.08.014
Status : Postprint (Author's version)

[20] A. Munafò, Multi-scale Models and Computational Methods for Aerothermodynamics, Ph.D. thesis Ecole Centrale Paris, 2014.

[21] A. Turchi, B. Helber, A. Munafò, T.E. Magin, Development and testing of an ablation model based on plasma wind tunnel experiments, 11th AIAA/ASME Joint Thermophysics and Heat Transfer Conference, 2014 AIAA 2014-2123, Atlanta, GA.

[22] P. Schrooyen, K. Hillewaert, T.E. Magin, P. Chatelain, Discontinuous Galerkin discretization coupled with sharp interface method for ablative materials, 21st AIAA Computational Fluid Dynamics Conference, 2013 no. AIAA 2013-2457, San Diego, CA.

[23] P. Schrooyen, Numerical Simulation of Aerothermal Flows through Ablative Thermal Protection Systems, Ph.D. thesis Universite catholique de Louvain, 2015.

[24] A. Munafò, T. Magin, Modeling of stagnation-line nonequilibrium flows by means of quantum based collisional models, Phys. Fluids 26 (9). doi:10.1063/1.4894842.

[25] A. Klomfass, S. Muller, Calculation of stagnation streamline quantities in hypersonic blunt body flows, Shock Waves 7 (1) (1997) 13–23, https://doi.org/10.1007/s001930050057.

[26] J. Scoggins, T. Magin, Gibbs function continuation for linearly constrained multiphase equilibria, Combust. Flame 162 (2015) 4514–4522, https://doi.org/10.1016/j.combustflame.2015.08.027.

[27] B.J. McBride, S. Gordon, Computer Program for Calculation of Complex Chemical Equilibrium Compositions and Applications: I. Analysis, National Aeronautics and Space Administration, Lewis Research Center, Cleveland, Ohio, October 1994 44135-3191, NASA Reference Publication, RP-1311.

[28] C. Park, R.L. Jaffe, H. Partridge, Chemical-kinetic parameters of hyperbolic earth entry, J. Thermophys. Heat Tran. 15 (1) (2001) 76–90, https://doi.org/10.2514/2.6582.

[29] Y.K. Chen, F.S. Milos, Navier-Stokes solutions with finite rate ablation for planetary mission earth reentries, J. Spacecraft Rockets 42 (6) (2005) 961–970, https://doi.org/10.2514/1.12248.

[30] D. Olynick, Y. K. Chen, M. E. Tauber, Aerothermodynamics of the stardust sample return capsule, J. Spacecraft Rockets 36 (3). doi:10.2514/2.3466.

[31] G.V. Candler, R.W. MacCormack, Computation of weakly ionized hypersonic flows in thermochemical nonequilibrium, J. Thermophys. Heat Tran. 5 (3) (1991) 266–273, https://doi.org/10.2514/3.260.

[32] W. Reed, T. Hill, Triangular Mesh Methods for the Neutron Transport Equation, Contractor Report LA-UR-73-479, Los Alamos Scientific Laboratory, June 1973.

[33] B. Cockburn, G. Karniadakis, C.-W. Shu, The development of discontinuous Galerkin methods, in: B. Cockburn, G.E. Karniadakis, C.-W. Shu (Eds.), Discontinuous Galerkin Methods, Springer, 2000, pp. 3–50.

[34] A. Bhatia, S. Roy, Pyrolysis gas flow in thermally ablating media using time-implicit discontinuous Galerkin methods, 49th AIAA Aerospace Sciences Meeting Including the New Horizons Forum and Aerospace Exposition, 2011 no. AIAA 2011-145, Orlando, FL.

[35] A. Bhatia, Application of Parallel Time-implicit Discontinuous Galerkin Finite Element Methods to Hypersonic Nonequilibrium Flow Problems, Ph.D. thesis University of Florida, 2014.

[36] A. Bhathia, S. Roy, R. Gosse, Effect of dielectric barrier discharge plasma actuators on non-equilibrium hypersonic flows, J. Appl. Phys. 116 (16) (2014) 1–11, https://doi.org/10.1063/1.4898862.

[37] H. Goldstein, Kinetics of Nylon and Phenolic Pyrolysis, Contractor Report, Lockheed Missiles and Space Company, October 1965.

[38] J. Brogan, A Numerical Method of Solution for Heat Conduction in Composite Slabs with a Receding Surface, Technical Report LMSD 288204 Lockheed Aircraft Corp, April 1960.

Published in : International Journal of Thermal Sciences (2018), vol. 134, pp. 639–652
DOI: https://doi.org/10.1016/j.ijthermalsci.2018.08.014
Status : Postprint (Author's version)

[39] C.B. Moyer, R.A. Rindal, An Analysis of the Coupled Chemically Reacting Boundary Layer and Charring Ablator. Part 2 - Finite Difference Solution for the In-depth Response of Charring Materials Considering Surface Chemical and Energy Balances,Contractor Report CR-1061, NASA, June 1968.

[40] V. Alexiades, G. Amiez, P. Gremaud, Super-time-stepping acceleration explicit schemes for parabolic problems, Commun. Numer. Meth. Eng. 12 (1996) 12–31, https://doi.org/10.1002/(SICI)1099-0887(199601)12:1<31::AID-CNM950>3.0.CO;2-5.

[41] J. Lachaud, A. Martin, I. Cozmuta, B. Laub, Ablation workshop test case, 4th Ablation Workshop, Albuquerque, New Mexico, 2011.

[42] J. Lachaud, A. Martin, T. Van Eekelen, I. Cozmuta, Ablation test-case series # 2, 5th Ablation Workshop, Lexington, Kentucky, 2012.

[43] G. Palmer, M. Barnhardt, B. Kirk, A. Amar, Y.-K. Chen, N. Mansour, Coupled CFD-ablation response model simulations using the libMesh framework, 11th AIAA/ASME Joint Thermophysics and Heat Transfer, 2014 no. AIAA 2014-2123, Atlanta, GA.

[44] R. Conti, R.W. MacCormack, L. Groener, J. Fryer, Practical Navier-Stokes computation of axisymmetric reentry flow fields with coupled ablation and shape change, 30th Aerospace Sciences Meeting and Exhibit, 1992 no. AIAA 1992-0752, Reno, NV.

[45] A. Martin, I.D. Boyd, Strongly coupled computation of material response and nonequilibrium flow for hypersonic ablation, J. Spacecraft Rockets 52 (1) (2015) 89–104, https://doi.org/10.2514/1.A32847.

[46] D. Kuntz, B. Hassan, D. Potter, Prediction of ablating hypersonic vehicles using an iterative coupled fluid/thermal approach, J. Thermophys. Heat Tran. 15 (2) (2001) 129–139, https://doi.org/10.2514/2.6594.

[47] Y.-K. Chen, T. Gökçen, Effect of non-equilibrium surface thermochemistry in simulation of carbon based ablators, J. Spacecraft Rockets 50 (5) (2013) 917–926, https://doi.org/10.2514/1.A32451.

[48] H. Alkandry, I.D. Boyd, A. Martin, Coupled flow field simulations of charring ablators with nonequilibrium surface chemistry, 44th AIAA Thermophysics Conference, 2013 no. AIAA 2013-2634, San Diego, CA.

[49] B. Helber, A. Turchi, O. Chazot, T.E. Magin, A. Hubin, Gas/surface interaction study of low-density ablators in sub-and supersonic plasmas, 11th AIAA/ASME Joint Thermophysics and Heat Transfer Conference, 2014 no. AIAA 2014-2122, Atlanta, GA.

[50] B. Bottin, O. Chazot, M. Carbonaro, V. van der Haegen, S. Paris, The VKI Plasmatron Characteristics and Performance, Contractor Report RTO EN-8, Los Alamos Scientific Laboratory, June 1999.

[51] B. Helber, A. Turchi, J.B. Scoggins, A. Hubin, T.E. Magin, Experimental investigation of ablation and pyrolysis processes of carbon-phenolic ablators in atmospheric entry plasmas, Int. J. Heat Mass Tran. 100 (2016) 810–824, https://doi.org/10.1016/j.ijheatmasstransfer.2016.04.072.

[52] B. Helber, Material Response Characterization of Low-density Ablators in Atmospheric Entry Plasmas, Ph.D. thesis Vrije Universiteit Brussel, von Karman Institute for Fluid Dynamics, 2016.

[53] Calcarb Rigid Carbon thermal Insulation, Technical guide HT 29 GB 0121, Mersen.

[54] P. Barbante, O. Chazot, Flight extrapolation of plasma wind tunnel stagnation region flowfield, J. Thermophys. Heat Tran. 20 (3) (2006) 493–499, https://doi.org/10.2514/1.17185.

[55] F. Wang, L. Cheng, H. Mei, Q. Zhang, L. Zhang, Effect of surface microstructures on the infrared emissivity of graphite, Int. J. Thermophys. 35 (2014) 62–75, https://doi.org/10.1007/s10765-013-1533-9.

[56] G.L. Vignoles, A. Turchi, D. Bianchi, P. Blaineau, X. Lamboley, D.L.Q. Huy, C. Levet, O. Caty, O. Chazot, Ablative and catalytic behavior of carbon-based porous thermal protection materials in nitrogen plasmas, Carbon 134 (2018) 376–390, https://doi.org/10.1016/j.carbon.2018.03.087.

Published in : International Journal of Thermal Sciences (2018), vol. 134, pp. 639–652
DOI: https://doi.org/10.1016/j.ijthermalsci.2018.08.014
Status : Postprint (Author's version)

[57] V.J. Murray, B.C. Marshall, P.J. Woodburn, T.K. Minton, Inelastic and reactive scattering dynamics of hyperthermal o and o2 on hot vitreous carbon surfaces, J. Phys. Chem. C 119 (26) (2015) 14780–14796, https://doi.org/10.1021/acs.jpcc.5b00924.

[58] David Driver, Michael Olson, Michael Barnhardt, Matthew MacLean, Understanding high recession rates of carbon ablators seen in shear tests in an arc jet, 48th AIAA Aerospace Sciences Meeting Including the New Horizons Forum and Aerospace Exposition, 2010 no. AIAA 2010–1177, Orlando, LA.

[59] A. Turchi, P.M. Congedo, T.E. Magin, Thermochemical ablation modeling forward uncertainty analysis—Part I: numerical methods and effect of model parameters, Int. J. Therm. Sci. 118 (2017) 497–509, https://doi.org/10.1016/j.ijthermalsci.2017.04.004.

[60] A. Turchi, P.M. Congedo, B. Helber, T.E. Magin, Thermochemical ablation modelling forward uncertainty analysis—Part II: application to plasma wind-tunnel testing, Int. J. Therm. Sci. 118 (2017) 510–517, https://doi.org/10.1016/j.ijthermalsci.2017.04.005.

[61] R.J. Willey, Comparison of kinetic models for atom recombination on high-temperature reusable surface insulation, J. Thermophys. Heat Tran. 7 (1) (1993) 55–62, https://doi.org/10.2514/3.11569.

[62] E.J. Jumper, W.A. Seward, Model for oxygen recombination on reaction-cured glass, J. Thermophys. Heat Tran. 8 (3) (1994) 460–465, https://doi.org/10.2514/3.565.

[63] F. Nasuti, M. Barbato, C. Bruno, Material-dependent catalytic recombination modeling for hypersonic flows, J. Thermophys. Heat Tran. 10 (1) (1996) 131–136, https://doi.org/10.2514/3.763.

[64] M. Balat-Pichelin, Interaction of Reactive Gas Flows and Ceramics at High Temperature - Experimental Methods for the Measurement of Species Recombination during Planetary Entry, Educational Notes RTO-en-avt-142, in Experiment, Modeling and Simulation of Gas-surface Interactions for Reactive Flows in Hypersonic Flights.

Published in : International Journal of Thermal Sciences (2018), vol. 134, pp. 639–652
DOI: https://doi.org/10.1016/j.ijthermalsci.2018.08.014
Status : Postprint (Author's version)

Nomenclature

F : convective flux vector

U : conservative variable vector

$\tilde{S}$: source term vector

F^{d}: diffusive flux vector

$\dot{m}$: surface mass blowing flux, kg/(m^{2}s)

B': dimensionless mass flow rate

C_H: Stanton number

C'_H : blowing-corrected Stanton number

C_M : mass transfer Stanton number

D_{eff}: effective diffusivity, m^2/s

E_a: activation energy, J/mol

H: static specific enthalpy, J/kg

h_{elem}: 1-D element size, m

k_{f}: reaction speed, m/s

M_{g} : molar mass

p: pressure, Pa

r: radial direction

S_{f}: specific surface, m^{-1}

t: time, s

T_h : Thiele number

x: stagnation-line direction

y: mass fraction

$\dot{S}$: recession velocity, m/s

e: specific energy, J/kg

h: enthalpy, J/kg

k: thermal conductivity, W/(mK)

N_{s}: number of gaseous species

N: number of solid components

$q_{\mathrm{cond,s}}$: conductive heat flux in the solid, W/m^2

q_{cond}: conductive heat flux in the gas, W/m^2

q_{conv}: convective heat flux in the gas, W/m^2

R: universal gas constant, 8.31J/(molK)

T: temperature, K

u: stagnation-line velocity, m/s

v: velocity normal to the stagnation line, m/s

GREEK SYMBOLS

ϕ: generic variable

θ: circumferential direction

$\dot{\omega}_{i_{\mathrm{g}}}$: overall surface pyrolysis source term of species $i$kg/(m^{2}s)

$\dot{\omega}_{i_{\mathrm{w}}}$: overall surface ablative source term of species $i$kg/(m^{2}s)

ϵ_{g}: gas volume fraction

K: permeability, m^2

λ: regime coefficient

μ: viscosity, kg/(ms)

Π: pyrolysis production rate, kg/(m^{3}s)

ρ_{0,s_i}: initial density of solid component i, kg/m^3

ρ_0: average initial density of solid matrix, kg/m^3

ρ_{r,s_i}: residual density of solid component i, kg/m^3

ρ_{s_i}: density of solid component i, kg/m^3

ρ: density, kg/m^3

σ: Stefan-Boltzmann constant, 5.67×10^{-8}W/(m^{2}K^4)

τ: stress tensor, kg/(m s^2)

ϵ: integral emissivity

Published in : International Journal of Thermal Sciences (2018), vol. 134, pp. 639–652
DOI: https://doi.org/10.1016/j.ijthermalsci.2018.08.014
Status : Postprint (Author's version)

SUBSCRIPTS

a: porous material

c: material in charred state

e: boundary-layer edge

f: fibers

g: pyrolysis gas

s: solid material

v: material in virgin state

w: gas-surface interface

∞: free stream

SUPERSCRIPTS

m: pyrolysis reaction parameter

r: gas-surface reaction